

Antonio Viviani, Andrea Aprovitola, Luigi Iuspa & Giuseppe Pezzella

Università della Campania "Luigi Vanvitelli", Dipartimento di Ingegneria, Via Roma 29, 81031, Aversa (CE), Italy

## **Abstract**

This work deals with the aerodynamic optimization of a fixed wing for a Mars concept-drone. The developed procedure aims to maximize the aerodynamic efficiency, modifying wing-sections at root and tip, as well as the sweep-angle, the taper-ratio, and the root-chord length. Specifically a maximum efficiency wing configuration, for a cruise flight segment in a range of angle of attack  $[0^{\circ},6^{\circ}]$  is searched at a Reynolds number of  $Re=60\times10^{3}$ . The total aircraft mass is supposed equal to 20 kg. To ensure consistent configurations, constraints on critical Mach number, wing mass, and pitching moment coefficient are applied. The optimization procedure uses a Free Form Deformation method along with parametric relations to define several reference airfoil sections of the wing. The parametric model also provides parameters to optimise the wing planform. Aerodynamic characteristics of airfoil, and of wing are calculated using the Xfoil and AVL solvers respectively. Subsonic conditions are assumed and compressibility effects are not accounted for. Single objective optimizations, carried out with a genetic algorithm supported by a Design Of Experiment and response surface, have been performed with different bounding limits. Results obtained in terms of different concept wings are illustrated and discussed.

Keywords: Wing optimization, Mars drone, Low-Reynolds flight.

# 1. Introduction

The recent development of technologies like Mars helicopters, exemplified by Ingenuity, has opened the way for a new dimension in planetary exploration by offering flexible solutions able to explore different types of terrain [1, 2]. Rovers like NASA's Curiosity and Perseverance provide precise, high-resolution images but are limited in coverage due to their slower movement across uneven terrain [3]. Orbiters, while capable of covering larger areas, offer lower image resolution, which might not suffice for an in-depth observation. A further solution to Mars exploration can be represented by fixed wing aircraft [4, 5].

Fixed-wing UAVs design will allow significant improvement for future Mars explorations for several reasons. During steady-level flight, fixed-wing UAVs are more efficient than rotor-craft, resulting in lower energy consumption. Additionally, when designed for maximum-efficiency cruise, propeller-driven UAVs can extend their endurance. Consequently, these configuration cover greater distances more quickly and efficiently than rotorcraft UAVs [6]. These aerial vehicles have also the advantage to facilitate more detailed local surface investigations, bridging the gap between the high-resolution capabilities of rovers and the broader coverage of orbiters. However, a wing designed for Martian exploration requires some specific aerodynamic optimization to ensure flight and manoeuvrability, considering factors like the lower density and gas composition of the Martian atmosphere.

Aircraft designed for Martian flight might need to operate at higher speeds compared to those on Earth to generate a comparable amount of lift due to the lower density. To generate the required aerodynamic force, a resulting Mach number of the order of  $M_{\infty}=0.6$  adds some additional complexity to the drone aerodynamic design. A different configuration to overcome the above mentioned problem is represented by a glider configuration. Gliding at low-Mach help avoid compressibility issues. Conversely, lower density coupled to the reduced aircraft size drives to aerodynamic challenges related to the low-speed flow regime. Specifically if the Reynolds number is of the order  $50 \times 10^3$  the shear layer separates in the laminar

regime [7]. This transition, particularly downstream of the separation point and near solid boundaries, significantly affects the aerodynamics of the aircraft. If the separated shear layer fails to reattach, it results in an extended wake region from the airfoil trailing-edge and an increase in pressure drag. Conversely, if reattachment occurs, it can form a long Laminar Separation Bubble (LSB), which can adversely affect the airfoil lift performance [8]. Laminar separation bubbles are highly unsteady and three-dimensional, due to the laminar bursting phenomena, and/or to a pre-stall condition. However, as outlined in Galbraith and Visbal [9] if the simulated angle of attack is small  $[0^{\circ}, 4^{\circ}]$ , the averaged in time effects of the laminar bubble can be considered steady. Therefore, feasible design conditions for design of a finite wing can be identified in this range accordingly. The pursuit of improving airfoil aerodynamic performance, particularly in the context of low Reynolds numbers and LSBs, has led to extensive efforts in modifying specific geometric features [10].

Airfoil optimization requires the designer to represent the aeroshape using a set of parameters that can be modified during a iterative process. Parametric methods play a crucial role, enabling precise manipulation of airfoil shapes. Two-dimensional methods such as B-Splines, Class/Shape function methods, and parametric techniques, like Free Form Deformation Methods, are commonly utilized within optimization procedures [11, 12], allowing for high accuracy and quality in shaping airfoil geometries. Specific geometric features, such as sharp Leading Edges (LEs), flat upper surfaces combined with concave undersides, and reduced thickness, are often considered as common criteria in trade-off studies for optimising airfoils intended for Martian flying explorers. These features can be effectively identified through optimization processes aimed at enhancing aerodynamic performance in Martian atmospheric conditions. Trade-offs and optimizations typically involve the balancing of various anthitetical factors such as lift, drag, stability, and manoeuvrability to design lifting surfaces that can perform efficiently within the unique Martian environment. This design approach is quite mandatory to achieve optimal aerodynamic performance for aircraft or gliders intended for exploration missions.

In this framework, Oyama and Fujii proposed a design procedure based on the airplane designed for future geographical exploration on Mars [13]. The objective of the design problem was the maximization of the lift-to-drag ratio in cruise condition at  $M_{\infty}=0.47$  and  $Re_{\infty}=10^5$ . Ayele and Maldonado [14] proposed a design of robotic ground-aerial vehicles for exploration missions to Mars prior to human arrival. Low-fidelity computational aerodynamic analyses were performed using OpenVSP to compute aerodynamic loads at a cruise Mach equal to 0.70.

Optimization loops driven by genetic algorithms are usually time consuming. Specifically, the evaluations of a drag polar for a finite wing, can be prohibitive within the framework of high fidelity Computational Fluid Dynamic methods. In a low-Reynolds flow the main efforts to predict the behaviour of LSB on various airfoil configurations stands in the a careful choice of the most appropriate turbulence model to correctly simulate LSB [7],[9], [15].

To reduce the computational overhead, low-level fidelity solvers like Xfoil and/or AVL can be adopted to build-up test-bed procedures evaluating aerodynamic coefficients at an affordable computational cost. The suitability of the Xfoil solver, and its validity for low-Reynolds applications, has been confirmed at  $Re = 20 \times 10^4$  by Morgado et al. [16], at  $Re = 60 \times 10^3$  by Aprovitola et al. [10], and at  $Re = 40 \times 10^3, 60 \times 10^3, 80 \times 10^3$  by Traub [17] respectively.

The present paper focuses on an aerodynamic optimization procedure for a wing, potentially suitable for a Martian exploration drone. The procedure is developed as a test-bed platform to explore the sensitivity of aerodynamic efficiency to the wing-section parameters, the sweep-angle, taper-ratio, and root chord length. The wing is supposed to perform a cruise flight with a Reynolds number related to mean aerodynamic chord equal to  $Re=60\times10^3$ . To explore the design space with consistent candidate shapes, constraints on critical Mach number, wing mass, and sign of pitching moment coefficient are assigned. The procedure integrates the free form deformation method, provided with a set of parametric relations, which defines the airfoil sections at the root, and tip of the wing sections. Results obtained with a genetic algorithm supported by a Design of Experiments and response surface methods are used to identify a range of candidate wings with distinct aerodynamic characteristics. Results assessment confirmed the reliability of the employed optimization framework.

# 2. Outline of Methodology

The outline of the design optimization procedure under investigation is depicted in the flowchart shown in Fig.1, The procedure is developed in ANSYS<sup>©</sup> Parametric Design Language (APDL) and is currently based on the following steps: i) airfoil parameterization; ii) aerodynamic computation; iii) optimization algorithm. The first step of the procedure involves the analysis of the sub-optimal wing section specifically tailored for low-Reynolds conditions. The wing design is performed through a two-step procedure. A laminar Eppler airfoil as a baseline wing-section used as starting configuration (A). First, the wing section design is performed in block (B) applying a Free Form Deformation (FFD) lattice which synchronously modifies the vertical displacement of several control points [10]. Control points are allowed to deform the pressure-side and the expansion side of the airfoil according to parametric relations.

In step (C) of the procedure, a parameterization for the wing planform is defined. Wing sections along

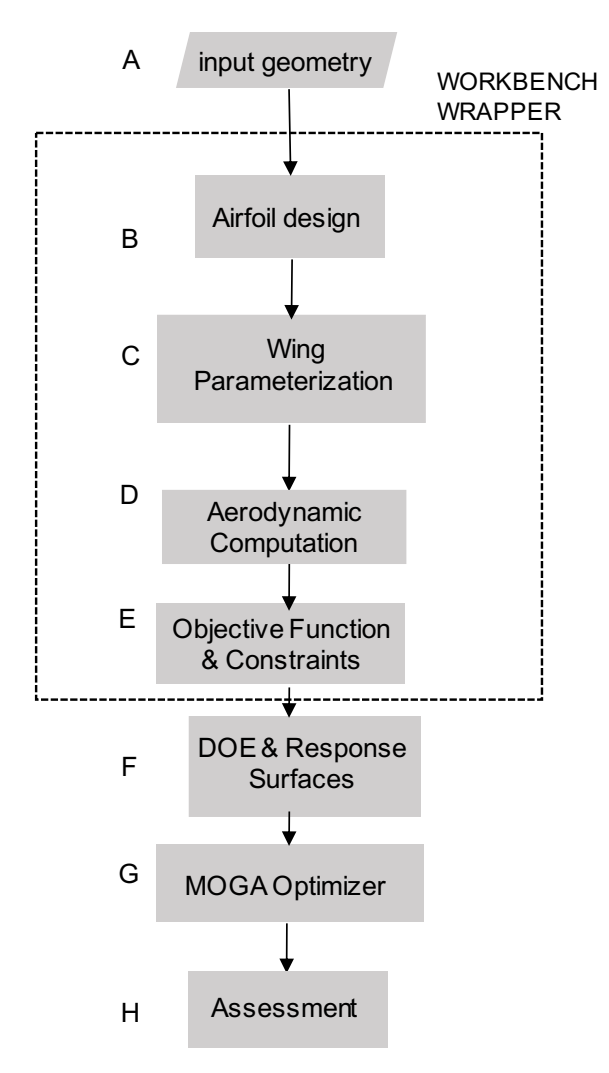


Figure 1 – Optimization procedure.

the span-wise direction are interpolated starting from specific root and tip airfoil instances controlled by the FFD-based parameterization algorithm. The wing planform is parametrically defined by assigning the taper-ratio  $\lambda$ , the sweep-angle  $\Lambda$ , the root chord length  $c_{root}$ , and the wing surface S.

The potential flow solver Xfoil and AVL are used to compute aerodynamic data in block (D) both for the single airfoil, and for the wing, to define design constraint (E). Specifically, Xfoil solver is used to compute the viscous drag coefficient of the wing section, related to the mean aerodynamic chord, at the zero-lift angle. On the other hand, AVL solver is used to complete the drag polar of the wing in the range  $[0^{\circ}, 6^{\circ}]$  where the linearity range is expected.

A Design of Experiment (DoE) and Response Surfaces generation is outlined in block (F). This way functional relations between input geometric parameters (3D wing instances) and the output (aerodynamic efficiency and/or other performance metrics), are resolved integrally with a very limited computational

cost by accepting a controlled level of approximation. This approach allows for a more streamlined and efficient optimization process by reducing the overall wall-clock time required to find optimal solutions. A Genetic Algorithm driven optimization for maximum efficiency objective is then carried out in block (G). Subsequent assessment phase (H) is finally performed to manage biased accuracy of response surfaces.

## 2.1 Airfoil parameterization

The Free-Form Deformation (FFD) method is a powerful tool utilised to achieve parametric variations of complex shapes [12, 18]. Essentially, by defining a modifiable lattice structure encompassing the initial shape of an object through a set of control points (CP), the deformation of the object can be achieved. This deformation is driven by the coordinates variation of the control points, which in turn deforms the lattice structure and its content. Through a series of parametric relations governing the position of these control points, the FFD method enables the exploration of local shape variations from a predetermined baseline configuration. Figure 2A-B illustrates this process visually. Assuming a two-dimensional control

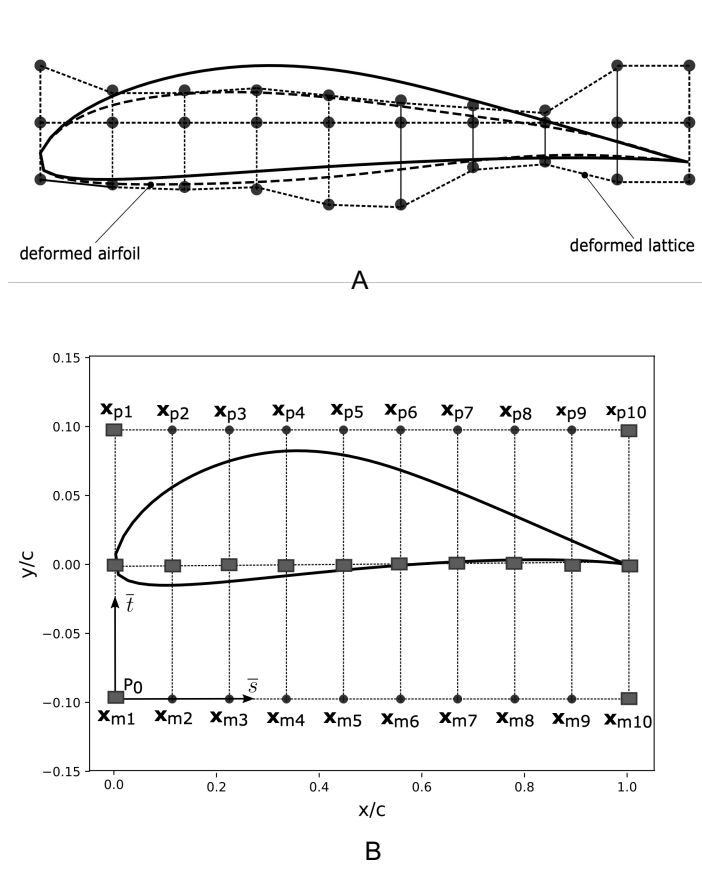


Figure 2 – Schematic representation of control lattice with deformed airfoil.

cage encompassing an airfoil, the lattice is defined such that its horizontal side equals the normalized chord length of the airfoil. The local frame of reference  $P_{0st}$  is established with its origin located at  $P_0(0,-(\tau+\delta))$  within the global frame of reference Oxy (see Fig.2B). Here,  $\tau$  represents the airfoil thickness, and  $\delta$  denotes the minimum distance between the horizontal top-side of the lattice and the airfoil.

The orientation of the control lattice is determined by vectors  $\overrightarrow{S}$  and  $\overrightarrow{T}$ . The position of any point within the lattice in the global coordinate system can be derived from its local coordinates (s,t).

$$\overrightarrow{P}(s,t) = \overrightarrow{P_0} + s\overrightarrow{S} + t\overrightarrow{T} \tag{1}$$

where s,t  $(0 \le s,t \le 1)$  are the local coordinates of point P. Shape deformation is commonly driven by a grid of  $(n+1) \times (m+1)$  control points  $P_{i,j}$  along the S, T axes:

$$\overrightarrow{P}_{i,j} = \overrightarrow{P_0} + \frac{i}{n}\overrightarrow{S} + \frac{j}{m}\overrightarrow{T}$$
 (2)

The variation in positions of FFD control points imposed by the change  $\Delta \overrightarrow{P}_{i,j}$  determines the deformation of the airfoil [10, 19]. To exclude unrealistic shapes, control points are synchronously moved on the top-side and the lower-side of the lattice, see Fig.3. Points  $(\mathbf{x}_{m1}, \mathbf{x}_{m10})$  and  $(\mathbf{x}_{p1}, \mathbf{x}_{p10})$  are kept fixed to preserve the chord length.

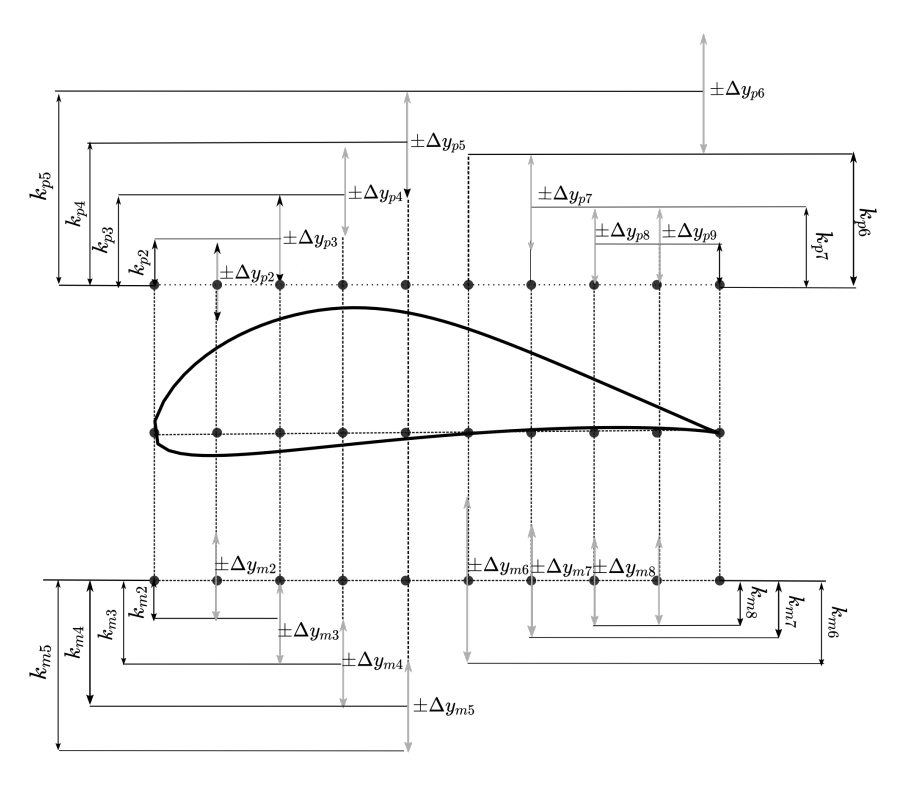


Figure 3 – Pictorial representation of Control lattice (top) and deformed airfoil (down).

Furthermore, the airfoil chord is placed at the half point of the vertical lattice side, and additional fixed control points are placed along this direction. Control points  $(\mathbf{x}_{m2},\ldots,\mathbf{x}_{m9})$  and  $(\mathbf{x}_{p2},\ldots,\mathbf{x}_{p9})$  on upper and lower side of the lattice, can be moved independently along the y-direction, but they are not allowed to move along the x direction. The y-coordinates of control points  $\mathbf{x}_{pi}(x_i,ky_{pi})$  and  $\mathbf{x}_{mi}(x_i,ky_{mi})$  are varied according to the following parametric relations:

$$\begin{cases} ky_{m_1} = 0 \\ ky_{m_2} = \Delta y_{m_2} \\ ky_{m_i} = ky_{m_{i-1}} + \Delta y_{m_i} & (i = 3, ..., 5) \\ ky_{m_j} = \Delta y_{m_j} & (j = 7, ..., 9) \\ ky_{m_{10}} = 0 \end{cases}$$

$$\begin{cases} ky_{p_1} = 0 \\ ky_{p_2} = \Delta y_{p_2} \\ ky_{p_i} = ky_{p_{i-1}} + \Delta y_{p_{i-1}} & (i = 3, ..., 9) \\ ky_{p_{10}} = 0 \end{cases}$$

where the displacements along y directions  $(\Delta y_{m_{i-1}}, \Delta y_{p_{i+1}})$  are respectively, chosen in order to have a maximum deviation from the baseline thickness shape equal to  $\Delta \tau = 1\%$  at  $Re_{\infty} = 60 \times 10^3$ .

# 2.2 Wing parameterization

Figure 4 shows a schematic representation of a wing, with the annotated geometrical parameters. The wing span b is expressed in terms of the wing-planform surface S, the root chord  $C_r$ , and the taper ratio  $\lambda$ :

$$\frac{b}{2} = \frac{S/2}{(C_r + C_r \lambda)} \tag{3}$$

Indicating with  $(X_{LET}, Y_{LET})$  the Leading Edge tip coordinates in the reference system shown in Fig.4,  $Y_{LET}$  is computed by the parametric relation:

$$Y_{LET} = \frac{C_r}{4} + \frac{b}{2}tan(\Lambda_{c/4}) - \frac{1}{4}(C_r\lambda)$$
(4)

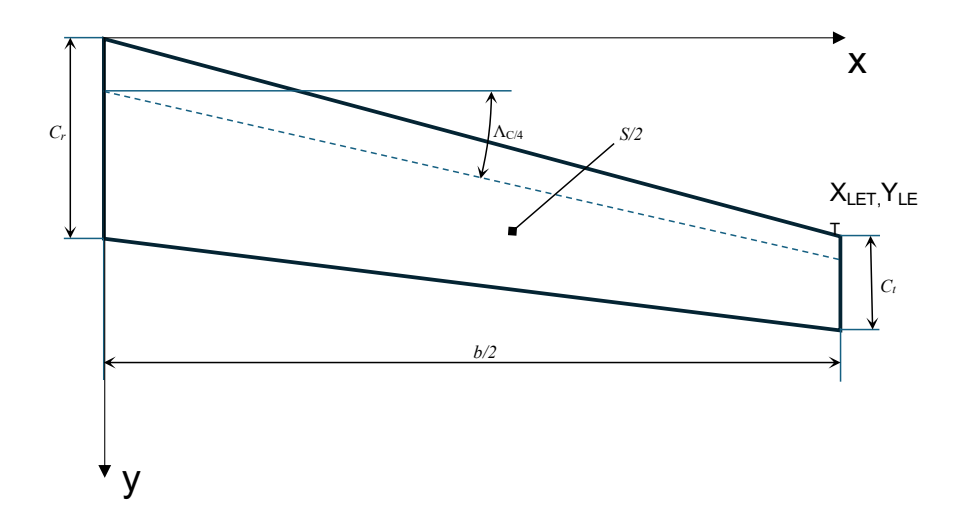


Figure 4 – Pictorial representation of the parametric wing planform.

# 3. Aerodynamic computation

# 3.1 Xfoil computations

Aerodynamic computations depicted in block D of Fig.1, are also performed using the Xfoil solver [20]. To account for flow transition, Xfoil simulations integrate the approximate  $e^N$  method. In the present computations, the default value of N is adopted for initial turbulence level [20, 16].

Two computations are performed: a first Xfoil run determines the drag contribution at zero-lift AoA  $C_{d,0}$  (i.e.  $C_l=0$ ), for the wing section, with a mean aerodynamic chord. A second run is performed to determine the minimum pressure coefficient  $Cp_0$ , at maximum lift coefficient of the wing in cruise condition. This value is then used in further steps of the procedure to formulate the optimization constraint on the critical Mach number.

# 3.2 AVL computations

The AVL code (Athena Vortex Lattice) is based on the VLM (Vortex Lattice Method). The VLM allows computing key aerodynamic properties such as lift distribution and induced drag for a specified wing configuration. In this method, the wing is described by a set of horseshoe vortices distributed along its span and chord, simplifying the complex airflow into a set of concentrated vorticity elements. This method neglects the effects of thickness and viscosity. In the current procedure AVL is adopted to compute the the lift and drag distribution in range  $[0^{\circ}, 6^{\circ}]$ . The total drag contribution is then obtained from parabolic drag polar:

$$C_D \approx C_{d,0} + \frac{C_L^2}{\pi A R e} \tag{5}$$

being  $AR = b^2/S$  the aspect ratio and e Oswald coefficient. The non-lifting drag contribution is supposed  $C_{D0} \approx C_{d,0}$  approximatively equal to the two-dimensional drag coefficient and assumed constant in the range  $[0^\circ, 6^\circ]$ . This simplificative assumption is used to avoid deadlock in the optimization procedure due to the convergence failure of Xfoil viscous computation.

## 4. Bounding limits and physical constraint

The cruise speed  $V_{eff}$  is obtained assuming equilibrium between the total weight of the vehicle  $W=nM_{tot}g_{Mars}$ , and the lift force created by the wing,  $L=C_{L(E)_{max}}q_{\infty}$ , being  $C_{L(E)_{max}}$  the lift coefficient at maximum efficiency,  $q_{\infty}=1/2\rho_{\infty}S_{wing}V_{eff}^2$  and given by:

$$V_{eff} = \sqrt{\frac{2nM_{tot}g_{Mars}}{C_{L(E)_{max}}S_{wing}\rho_{\infty}}}$$
 (6)

, and the effective cruise Mach number  $M_{eff}=V_{eff}/a_{\infty}$  is defined accordingly. In the current procedure compressibility effects are not taken into account. The above mentioned conditions is verified if  $M_{eff}\leq$ 

 $M_{cr}$ ,  $M_{cr}$  being the critical Mach number. The value of  $M_{cr}$  for  $M_{\infty} \in [0,1]$  is determined by computing the intersection between the expression of pressure coefficient by the Prandtl-Glauert relation

$$C_p = \frac{C_{p0}}{\sqrt{1 - M_{\infty}}} \tag{7}$$

and the isentropic pressure coefficient:

$$C_{pcr} = \frac{2}{\gamma M_{\infty}^2} \left[ \left( \frac{(2 + (\gamma - 1)M_{\infty}^2)}{\gamma + 1} \right)^{\frac{\gamma}{\gamma - 1}} - 1 \right]$$
 (8)

 $\gamma=1.32$  being the specific heat-ratio of Mars atmosphere. Therefore the compressibility limit is formulated as  $C_{costr}=\frac{M_{eff}}{M_{crit}}\leq 1$ . Additionally, a bounding limit related to the maximum mass of the wing  $M_{wing}$  is adopted. Assuming a total vehicle mass  $M_{tot}=20kg$ , it is supposed that  $M_{wing}$  should not exceed 20 % of  $M_{tot}$ .

# 5. Wing Optimization

The optimization problem assumes to maximise aerodynamic efficiency of a wing of a concept drone having mass  $M_{tot}$  =20kg in the range of AoA  $[0^{\circ}, 6^{\circ}]$  supposed for a cruise flight phase.

## 5.1 Problem formulation

The computational procedure of Fig.1 is applied in two single-objective optimizations denoted in the following as  $\mathbf{Opt}_{\mathbf{I}}\mathbf{I}$  and  $\mathbf{Opt}_{\mathbf{I}}\mathbf{I}$ , respectively. The general formulation of the optimization problem is described as follows:

$$\begin{cases}
 max f(\mathbf{x}); & \mathbf{x} = (x_1, \dots, x_n) \\
 \underline{x}_i \le x_i \le \overline{x}_i & i = 1, n \\
 \underline{g}_j \le g_j(\mathbf{x}) \le \overline{g}_j & j = 1, k
\end{cases} \tag{9}$$

 ${f x}$  being the vector of design variables and  $g_j$  and  $\overline{g_j}$  the j-th constraints.

dV	Symbol	Min. value	Max. value	Unit
$P_{p2}$	$\Delta y_{p2}$	-0.5	0.5	ad
$P_{p3}$	$\Delta y_{p3}$	0.0	0.6	ad
$P_{p4}$	$\Delta y_{p4}$	0.0	0.7	ad
$P_{p5}$	$\Delta y_{p5}$	0.0	0.2	ad
$\dot{P_{p6}}$	$\Delta y_{p6}$	-0.1	0.1	ad
$\hat{P_{p7}}$	$\Delta y_{p7}$	-0.1	0.1	ad
$P_{p8}$	$\Delta y_{p8}$	-0.1	0.1	ad
$P_{p9}$	$\Delta y_{p9}$	-0.1	0	ad
$P_{m2}$	$\Delta y_{m2}$	-1.0	0.2	ad
$P_{m3}$	$\Delta y_{m3}$	-1.0	0.5	ad
$P_{m4}$	$\Delta y_{m4}$	-1.0	0.5	ad
$P_{m5}$	$\Delta y_{m5}$	-1.0	0.5	ad
$P_{m6}$	$\Delta y_{m6}$	-1.0	1.0	ad
$P_{m7}$	$\Delta y_{m7}$	-1.0	1.0	ad
$P_{m8}$	$\Delta y_{m8}$	-1.0	1.0	ad
$P_{m9}$	$\Delta y_{m9}$	-1,0	1.0	ad

Table 1 – Side constraints for design variables (FFD-based parameterization) .

The same side constraints for wing-sections parameters are assumed in Opt\_I and Opt\_II and shown in Table 1. Objective function, design variables, and bounding limits of optimizations are summarised in Table 2 and Table 3 (Opt\_I) and in Table 4 and Table 5 (Opt\_II). In the optimization campaigns a DoE (Design of Experiment) with a Latin-Hypercube sampling method is performed to generate the search space of design parameters. The DOE was performed by generating 580 samples related to twenty design variables. Then a response surface is approximated with a 2nd order polynomial, to obtain the approximation of objective function and constraints.

Function name	Admissible range	
Aerodynamic Efficiency OBJ		Max in $\alpha \in [0^{\circ}, 6^{\circ}]$
Mach constraint	CST	$\leq 1 \text{ in } \alpha \in [0^{\circ}, 6^{\circ}]$
Mass Constraint	CST	$\leq 0.2$ in $\alpha \in [0^{\circ}, 6^{\circ}]$
Pitching moment	CST	$\leq 0$ in $lpha \in [0^\circ, 6^\circ]$

Table 2 – Opt\_I: Objective and bounding limits for optimization problem.

dV	Symbol Min. value		Max. value	Unit
Croot	$C_r$	0.4	1.1	m
Sweep	$\Lambda_{c/4}$	0°	$35^{\circ}$	deg
Taper ratio	$\lambda$	0.3	0.6	ad
Wing Surf.	S	2	5	$m^2$

Table  $3 - Opt_I$ : Side constraints for wing design variables.

Function name	Admissible range
Aerodynamic Efficiency OBJ	Max in $\alpha \in [0^{\circ}, 6^{\circ}]$
Critical Mach Constraint CST	$\leq 1$ in $\alpha \in [0^{\circ}, 6^{\circ}]$
Mass Constraint CST	$\leq 0.2$ in $\alpha \in [0^{\circ}, 6^{\circ}]$
$C_M$ Constraint CST	$\leq 0 \text{ in } \alpha \in [0^{\circ}, 6^{\circ}]$
b Constraint CST	$\leq 5m \text{ in } \alpha \in [0^{\circ}, 6^{\circ}]$

Table 4 – Opt\_II: Objective and bounding limits for optimization problem.

dV	Symbol	Min. value	Max. value	Unit
Croot	$C_r$	0.4	1.1	m
Sweep	$\Lambda_{c/4}$	0°	$35^{\circ}$	deg
Taper ratio	$\lambda$	0.3	0.6	ad
Wing Surf.	S	1.5	3	$m^2$

Table 5 – Opt II: Side constraints for wing design variables.

An optimization procedure based on floating-point version of MOGA implemented in ANSYS® Workbench, has been used to find the best wing geometry for maximum efficiency. The algorithm is initialised assuming a population of 1000 individuals for an adequate initial sampling of the search space. A population of 500 individuals is then defined for the iterative evolutionary process to assure a robust convergence of the algorithm. A convergence criterion of 2% on the stability of the population has been adopted.

## 5.2 Optimization results: Opt I

Wing	Symbol	Opt.	Unit
Croot	$C_r$	0.4	m
Sweep	$\Lambda_{c/4}$	$5.8^{\circ}$	deg
Taper ratio	$\lambda$	0.3	ad
Wing Surf.	S	2.7	$m^2$
Wigspan	b	10.2	m
Wing Mass	$M_{Wing}$	3.9	kg
Aer. Eff.	$(L/D)_{ma}$	<sub>x</sub> 41.3	ad
Oswald	e	0.95	ad
Max $C_L$	$C_{L(Emax)}$	1.3	ad

Table  $6 - \mathbf{Opt}_{\mathbf{I}}$ : Reference characteristics of optimal candidate .

In Figure 5A-D the convergence history of objective function and constraints for  $\mathbf{Opt}_{-}\mathbf{I}$  is shown. Convergence is reached after 9 generations which corresponds to 4950 evaluations of the objective function. The optimal candidate is shown in Fig.6C,D and in Table 6 its reference characteristics are reported. The optimal candidate attains the maximum efficiency  $(L/D)_{max}=41.3$  with a wingspan b=10 m and a

sweep-angle  $\Lambda_{c/4}=5^\circ$  (see Tab.6). The design exploration trend is also confirmed in Fig.5B where it is shown that the compressibility constraint is not engaged at all, being the cruise flight  $V_{eff}$ =54.7 m/s. In Fig.5E and Fig.5F the convergence history of root chord  $C_r$  and of the sweep angle  $\Lambda_{c/4}$  are shown. Specifically, it can be noted that, while the  $C_r$  value appears to be early stabilized, value of  $\Lambda_{c/4}$  is repeatedly updated due to increasing of b during convergence of optimization. Therefore, provided the described set of constraints, the procedure finds an expected positive correlation between the value of b and b0 and b1 and b2 are figure 6 shows the lift distribution for the optimal candidate, with maximum aerodynamic load distributed on the wing centerline.

Finally, in Fig.6B a comparison between the Eppler E387 airfoil and the optimised airfoil is shown. Figure 6B points out that the optimal airfoil, has different geometrical features if compared to the E387 airfoil on the suction side. A lower thickness  $\tau_{max}=8.81\%$  (@31%c) and a lower camber  $\gamma_{max}=2.56\%$  (@35%c) compared to the E387 airfoil is observed. Despite the approximate viscous solution given by the Xfoil solver, the main effect of low-Reynolds number seems to be accounted for in the optimization results. On one hand, comparisons between low-Reynolds CFD simulations in literature between E387 and different airfoils shows that the increased curvature increase on the pressure side is beneficial for flow reattachment, because it increases the expansion on the suction side [7, 10, 17]. Such a feature can be also observed in Fig.6B. On the other hand, the expansion side of the optimal airfoil shows a smooth profile which is expected to allow laminar flow development. The maximum camber of the optimal airfoil appears shifted forward with respect to the E387, which is not in agreement with literature results on low-Reynolds airfoils. However, this effect requires deeper investigation with high fidelity Computational Fluid Dynamics simulation. Finally, as a cross check of the approximation introduced by assumption of parabolic drag polar Eq.5 states that at  $E_{max}$ 

$$C_{d,0} = \frac{C_L^2}{\pi A R e} \tag{10}$$

In the current computation  $C_L=(C_L)_{E_{max}}=C_{Lmax}=1.3$ , due to the linearity range. Therefore  $\frac{C_L^2}{\pi ARe}=0.014$  which results 20% lower than  $C_{d,0}=0.016$  predicted by Xfoil.

## 5.3 Optimization results: Opt II

In Figure 7A-F the convergence history of the objective function and constraints for Opt\_II is shown. Convergence is reached after 20 generations which corresponds to 10000 evaluations of the objective function. The optimal candidate is shown in Fig.8C,D while in Table 7 geometrical and aerodynamic features are reported. To address the exploration capability of the developed procedure an additional constraint on the wingspan length is adopted and shown in Table 5. Figure 8C and Fig. 8D points out that the optimal candidate has a greater value of  $\Lambda_{c/4}=32^{\circ}$  if compared to Opt\_I. This design trend is explained by considering that compressibility constraint  $C_{costr}$ , is verified with lower values of S (see Opt\_I). In fact the wing maximises efficiency flying at a higher speed i.e.  $V_{eff}=64$  m/s if compared to

Wing	Symbol	Opt.	Unit
Croot	$C_r$	0.6	m
Sweep	$\Lambda_{c/4}$	$32^{\circ}$	deg
Taper ratio	$\lambda$	0.3	ad
Wing Surf.	S	1.8	$m^2$
Wigspan	b	4.74	m
Wing Mass	$M_{Wing}$	3.3	kg
Aer. Eff.	$(L/D)_{ma}$	<sub>x</sub> 31.4	ad
Oswald	e	0.96	ad
Max $C_L$	$C_{L(Emax)}$	0.82	ad

Table 7 – Opt\_II: Reference characteristics of optimal candidate.

the previous run. This evidence is also confirmed comparing convergence histories of  $C_{costr}$  in Fig.7B with Fig.5B. Additionally, having constrained the wingspan, a wing with b=4.74 m and  $(L/D)_{max}=31.4$  is obtained (see Tab.7). These results evidence a consistent feedback of the additional constraint adopted, over the shape of optimal candidate. Therefore, the procedure is sensitive to search different regions of the search space. Figure 8A shows the lift force distribution of the optimal candidate. The high sweep and the

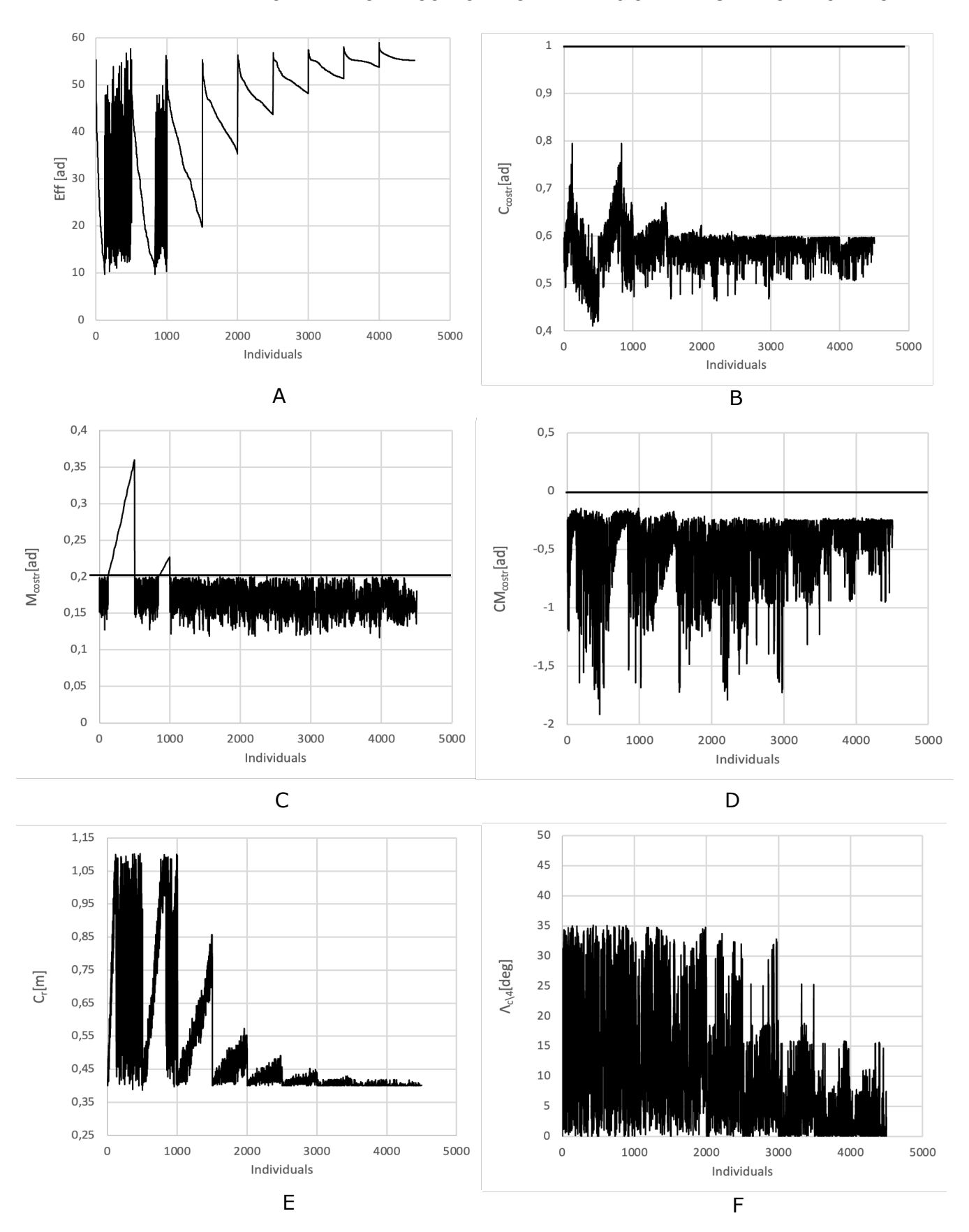


Figure 5 – Convergence history for optimization Opt\_I: (A) Objective function; (B) Critical Mach constraint; (C) Mass Constraint; (D) Pitching Moment constraint; (E) Root chord; (F) Sweep angle.

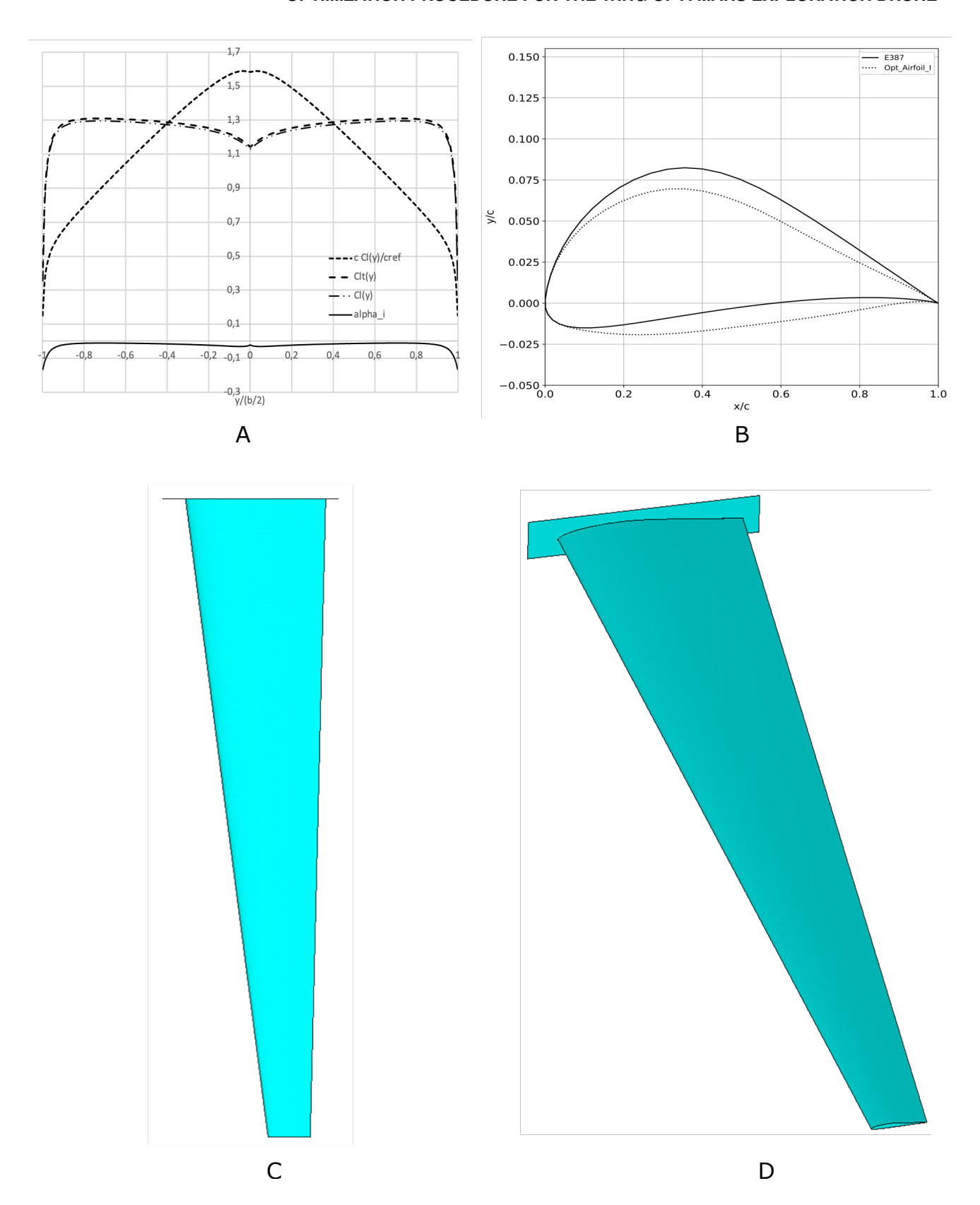


Figure 6 – Opt\_I: (A) Surface force distribution; (B) Optimized airfoil; (C) Optimised Wing (Top-view); (D) Optimised Wing (oblique-view).

short wingspan (nearly half compared to the Opt\_I result), redistributes the aerodynamic load toward the wingtips. Such design of wing-planform in a low-density environment suggests an adoption of propulsion system. Figure 8B shows the comparison of the optimal airfoil with the E387. It can be observed that

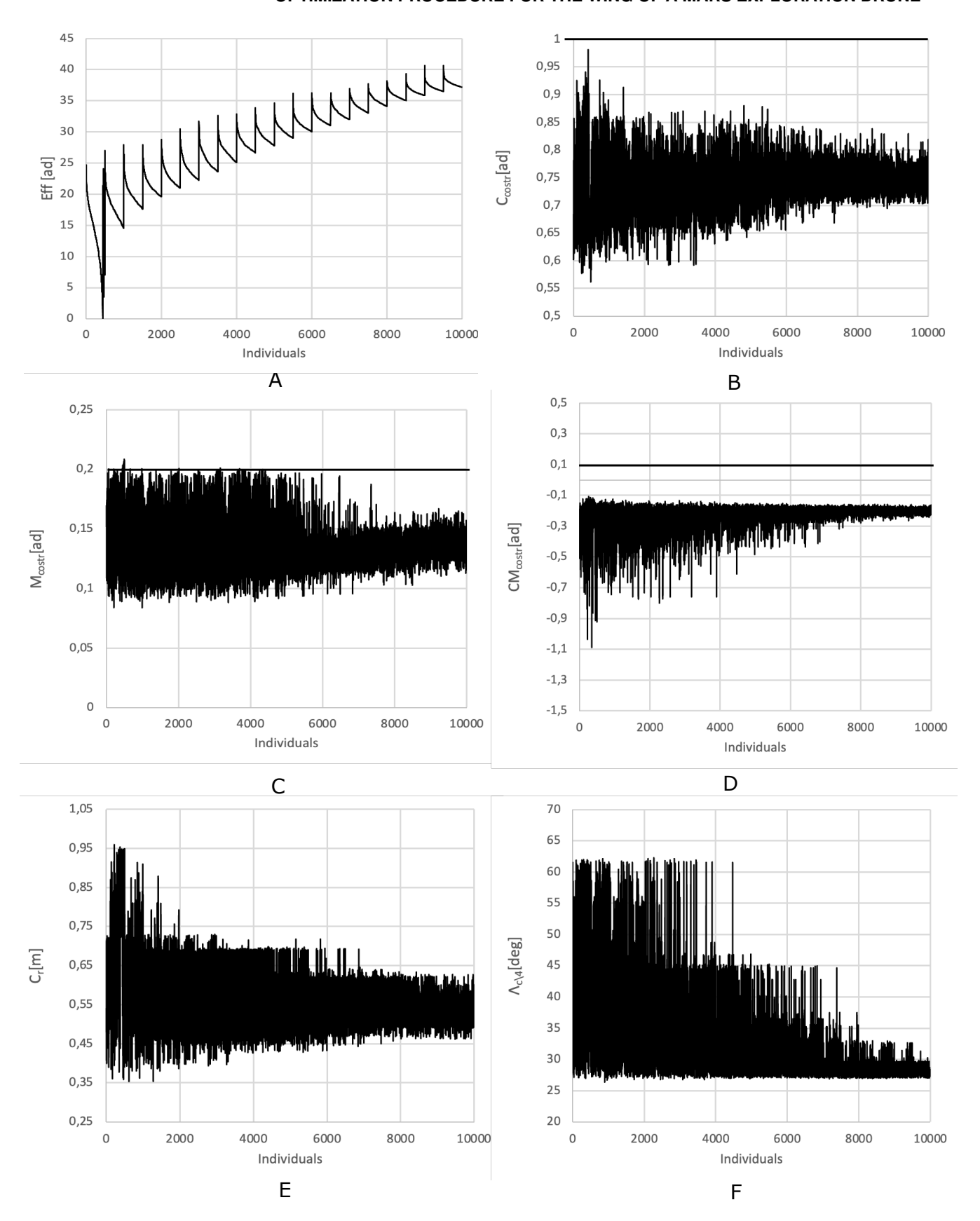


Figure 7 – Opt\_II: Convergence history-(A) Objective function; (B) Compressibility constraint; (C) Mass constraint; (D) Pitching moment; (E) Root chord; (F) Sweep Angle.

for Opt\_II the design exploration, tends to maximize efficiency by penalizing the total drag. In fact the optimal airfoil of the wing shows a larger curvature  $\gamma=6\%$  @40% chord both on the suction side and on

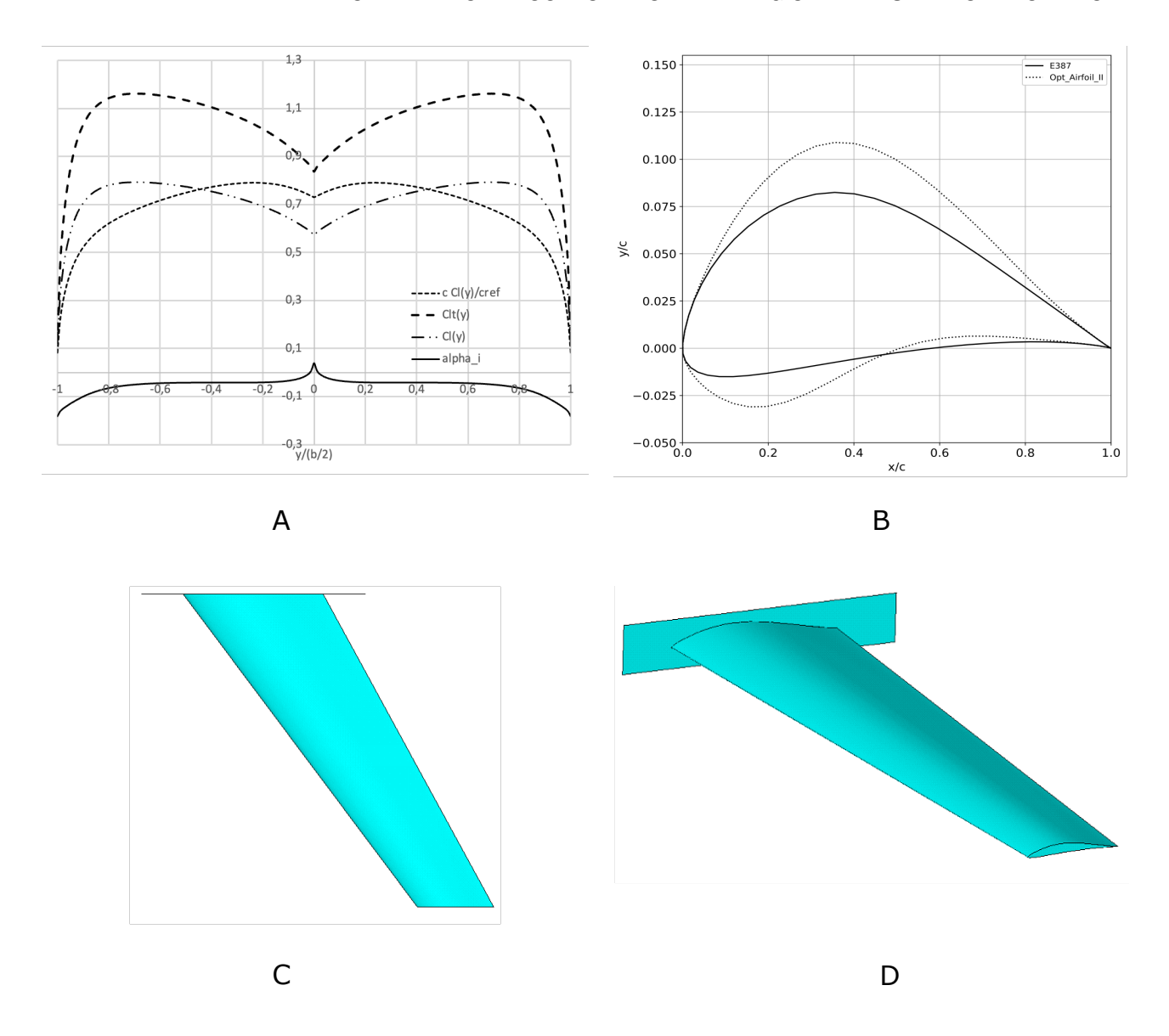


Figure 8 – Opt\_II: (A) Surface force distribution; (B) Optimized airfoil; (C) Optimised Wing (top-view); (B) Optimised Wing (oblique-view).

the pressure side, and  $\tau_{max}=11\%$  @34% chord which leads to a value of profile drag  $C_{d,0}=0.028$ 

# 6. Conclusions

In this study an aerodynamic optimization for a wing of a Mars concept-drone was shown. An in-house developed optimization procedure, capable to vary the shape of airfoil and of wing planform, has been developed. The procedure has proven to be effective to maximise aerodynamic efficiency by varying the main wing design parameters. Single-objective optimizations for a maximum efficiency shown that, despite the approximate solution provided by the low-fidelity panel flow-solvers, optimal configurations reflected some peculiarity of the low-Reynolds number regime. Different optimal shapes were obtained depending on specific constraints added to the problem formulation. Specifically, larger wingspans are associated with low-curvature, low-thickness airfoils. Differently high swept-wings are associated with more curved airfoil shape at tip and root, which penalise the drag-coefficient, but allows higher cruise speeds. This work can be assumed as a preliminary exploration for future studies and optimizations in the context of low-density, low-Reynolds Martian flight environment.

## 7. Contact Author Email Address

mailto: antonio.viviani@unicampania.it (corresponding author)

# 8. Copyright Statement

The authors confirm that they, and/or their company or organization, hold copyright on all of the original material included in this paper. The authors also confirm that they have obtained permission, from the copyright holder of any third party material included in this paper, to publish it as part of their paper. The authors confirm that they give permission, or have obtained permission from the copyright holder of this paper, for the publication and distribution of this paper as part of the ICAS proceedings or as individual off-prints from the proceedings.

#### References

- [1] Balaram J and Tokumaru P T. Rotorcraft for Mars exploration. *In 11th International Planetary probe Workshop*, Pasadena, California, June 16-20,2014.
- [2] Barlow N. *Mars: an introduction to its interior, surface and atmosphere*. Cambridge University Press, New York, 2014.
- [3] Bouskela A, Kling A, Schuler T, Shkarayev S, Kalita H, and Thangavelautham J. Mars exploration using sailplanes. *Aerospace, MDPI*, Vol. 9, No. 306, 2022.
- [4] Engineering National Academies of Sciences and Medicine. Visions into voyages for planetary science in the decade 2013–2022: A midterm review. *The National Academies Press:Washington, DC, USA*, 2018.
- [5] National Research Council. Vision and voyages for planetary science in the decade 2013–2022. *The National Academies Press:Washington, DC, USA*, 2021.
- [6] Hassanalian M, Rice D, and Abdekelefi A. Evolution of space drones for planetary exploration: a review. *Progress in Aerospace Science*. Vol. 97, 2018.
- [7] Winslow J, Otsuka H, Govindarajan B, and Chopra I. Basic understanding of airfoil characteristics at low Reynolds Numbers (10<sup>4</sup>-10<sup>5</sup>). *Journal of Aircraft, Vol.55*. No. 3, 2018.
- [8] Clara D S, Catalano P, Tognaccini R. Model for enhancing turbulence production in laminar separation bubbles, *AIAA Journal*, Vol. 60, No. 1, 2022.
- [9] Galbraith M C and Visbal M R. Implicit large eddy simulation of low-Reynolds-number transitional flow past the SD7003 airfoil. *In: 40th AIAA Fluid Dynamics Conference and Exhibition*, Reno Nevada, 7-12 January 2008. (AIAA) 2008-225.
- [10] Aprovitola A, Iuspa L, Pezzella G, and Viviani A. Aerodynamic optimization for airfoil shape for atmospheric flight on Mars planet, *Acta Astronautica*, vol. 212, 2023.
- [11] Sasaki G, Tatsukawa T, Nonomura T, Oyama A, Matsumoto T, and Yonemoto K. Multi-objective optimization of airfoil for Mars exploration aircraft using genetic algorithm. *Transaction JSASS Aerospace Tech*, Japan. 2014.
- [12] Sederberg T W and Parry S R. Free-form deformation of solid geometric models. *In: SIGGRAPH Comput. Graph. 20, Dallas*, Texas 18-22 August, 1986.
- [13] Oyama A and Fujii K. A study on aifoil design for future Mars airplane. *In: 44th AIAA Aerospace Sciences Meeting and Exhibition*, Reno Nevada, 09-12 january 2006. (AIAA) 2006-1484.
- [14] Ayele W and Maldonado V. Conceptual design of a robotic ground-aerial vehicle with an aeroelastic wing model for Mars planetary exploration, *Aerospace Astronaut*. 10 (404) (2023).
- [15] Catalano P and Tognaccini R. RANS analysis of the low-Reynolds number flow around the sd7003 airfoil. Aerospace Science and Technology, vol. 15, 2011.
- [16] Morgado J, Vizinho R, Silvestre M A R, and Pascoa J C. Xfoil vs CFD performance predictions for high lift low Reynolds number airfoils. *Aerospace Science and Technology*, Vol. 52, 2016.
- [17] Traub L W and Coffman C. Efficient Low-Reynolds-Number Airfoils. Journal of Aircraft, 56(6), 2019.
- [18] Shen Y, Huang W, and Yan L Zhang tian T. Constraint-based parameterization using FFD and multi-objective design optimization of a hypersonic vehicle. *Aerospace Science and Technology*, (100), 2020.
- [19] Magalhaes Junior J M, Halila G L O, Kim Y, Khamvilai T, and Vamvoudakis K G. Intelligent data-driven aerodynamic analysis and optimization of morphing configurations. *Aerospace Science and Technology*, Vol. 121, 2022.
- [20] Drela M. Xfoil an analysis and design system for low reynolds number airfoils. in: T.J. Mueller (Ed.) Low Reynolds Number Aerodynamics, Springer-Verlag. Berlin, pages 1–12, 1989.